Microscopic dielectric permittivities of graphene nanoribbons and graphene

Jingtian Fang, William G. Vandenberghe, and Massimo V. Fischetti
Department of Materials Science and Engineering, The University of Texas at Dallas, Richardson, Texas 75080, USA
(Received 19 May 2016; revised manuscript received 12 July 2016; published 28 July 2016)

We derive a microscopic Poisson equation using the density-density response function. This equation is valid for any realistic potential perturbation and permits the study of dielectric response in nanostructures, especially in one-dimensional nanostructures and quantum dots. We apply this equation to simulate a nanoscale parallel-plate capacitor (nanocapacitor) with graphene as dielectric and two nanocapacitors with a graphene nanoribbon (GNR) as dielectric. The density-density response function is calculated using first-order perturbation theory and empirical pseudopotentials. From the microscopic electric field of the graphene nanocapacitor, we calculate the out-of-plane microscopic dielectric constant of graphene and from the electric field of GNR nanocapacitors, we calculate the full microscopic dielectric tensor of several GNRs with different widths. We find that the out-of-plane microscopic dielectric constants of GNRs and graphene do not depend on their energy band gap. We also study the effect of a surrounding dielectric on the dielectric permittivity of graphene and we conclude that the surrounding dielectric barely affects the dielectric permittivity of graphene.

DOI: 10.1103/PhysRevB.94.045318

I. INTRODUCTION

The dielectric properties of low-dimensional nanostructures have attracted a broad scientific interest because of their crucial importance in determining the optical conductivity and transmittance of nanophotonic devices and electron transport properties of nanoelectronic transistors [1–14]. Both macroscopic and microscopic studies of the dielectric response of perturbed nanosystems have been performed and several methods have been developed [1–12]. The application of a uniform external electric field as the perturbation has been frequently used to calculate the atomic-scale dielectric permittivity of two-dimensional (2D) layered structures [1–4] and to compute the macroscopic transverse susceptibility tensor of one-dimensional (1D) carbon nanotubes [8,9,15]. A δ-like and a truncated Coulomb-like potential perturbations have been applied to study zero-dimensional (0D) quantum dots [5] and a core-shell charge perturbation was applied to study silicon spherical crystallites [1]. To study both the macroscopic and the microscopic dielectric response of bulk materials, Resta and Kunc [6,7] have proposed a periodically repeated capacitor subject to the potential perturbation of a constant field. A vanishing internal electric field with applying external dipole layer (i.e., "short-circuit" electrical boundary conditions) was applied in an *ab initio* study of ferroelectric thin-film perovskite compounds polarization [12]. An alternative way to study dielectric properties consists in calculating the dielectric matrix $\epsilon^{-1}_{\mathbf{GG'}}(\mathbf{q})$ through first-order perturbation theory and then determining the macroscopic dielectric constant or tensor from the matrix [13,14].

However, the use of the approaches mentioned above to calculate the microscopic dielectric tensor of 1D and 0D nanomaterials has not been reported, to the best of our knowledge. One particular instance showing the importance of the microscopic dielectric tensor of low-dimensional nanostructures is its appearance in the Poisson equation that must be solved self-consistently in atomistic quantum-transport studies [16–23]. Several authors [20–23] have simulated quantum electron transport in graphene nanoribbon (GNR) field-effect transistors atomistically by solving the Schrödinger equation and the "ordinary" Poisson equation $\nabla \cdot [\epsilon(\mathbf{r})\nabla\varphi_{\text{tot}}(\mathbf{r})] = -\rho_{\text{ext}}(\mathbf{r})$, self-consistently, where $\epsilon(\mathbf{r})$ is the dielectric constant of the channel material or the surrounding oxide, $\varphi_{\text{tot}}(\mathbf{r})$ is the total potential, and $\rho_{\text{ext}}(\mathbf{r})$ is free charge density. However, the Poisson equation was solved in a macroscopically crude way, either arbitrarily assuming a uniform dielectric constant throughout the entire device [18,20], or assuming one dielectric constant for the channel material and another for the oxide while defining the interface as "straight ϵ-discontinuity lines," lines arbitrarily drawn among atoms ("box assumption") [21–23]. Thus, the physical dielectric response is not properly accounted for in these simulations. The aforementioned atomic-scale dielectric permittivity of 2D layered structures [1–4] may provide some guidance to determine the thickness of an assumed uniform dielectric for 2D materials and validate the box assumption. Nevertheless, atomistic dielectric permittivities for 1D and 0D structures are currently not available.

Methodologically, the idea of applying a uniform external electric field to study the dielectric response of low-dimensional nanostructures is questionable for two reasons. First, when using a plane-wave basis, the periodic boundary conditions of the supercell approach introduce an artificial perturbation from image dipoles ("supercell artifact") [9,12,24]. Dipole corrections [25], the application of a large vacuum region in the supercell [9,26] and/or a truncated Coulomb kernel [27], are the typical methods used in density-functional theory and GW calculations that aim at minimizing/removing the image interactions and the artificial electric field. The second reason originates from the physical fact that the displacement field is nonuniform in an inhomogeneous system composed of 1D or 0D nanomaterials and the surrounding dielectric. Therefore, the approach used for bulk materials and 2D materials cannot be directly extended to 1D and 0D nanostructures [5,8–11].

In this paper we derive a microscopic Poisson equation based on the density-density response function [28,29] and study the static dielectric properties of armchair-edge GNRs (aGNRs). We introduce nanoscale parallel-plate capacitors (nanocapacitors) with aGNR dielectrics. We apply physically realistic boundary conditions by imposing a voltage

bias between capacitor plates. This results in a nonuniform electric-field perturbation in the nanosystems. By solving the microscopic Poisson equation for two nanocapacitors with their plates along different orientations with respect to the aGNR surface, we are able to calculate the full microscopic dielectric tensor. Next, we also compute the microscopic dielectric constant of graphene and compare it with the dielectric constant of several aGNRs. We find that the out-of-plane microscopic dielectric constants of aGNRs and graphene do not show a band-gap dependence. Finally, we study the effect of hexagonal boron nitride (hBN) on the dielectric constant of graphene and find that the presence of hBN barely affects the permittivity of graphene. In our methodology, the supercell artifact is avoided since the density-density response function decays exponentially with the spatial decay of the valence electron density. By employing empirical pseudopotentials and supercells with suitable sizes, we are able to reduce the size of the plane-wave basis and the associated computational burden.

The paper is organized as follows. Section II introduces the density-density response function and proceeds with the derivation of the microscopic Poisson equation. We present the microscopic dielectric tensor of an aGNR in Sec. III A, the ribbon-width dependence of the dielectric constant in Sec. III B, and the out-of-plane microscopic dielectric constant of graphene in Sec. III C. We study the effect of hBN on graphene in Sec. III D. We conclude the paper in Sec. IV.

II. COMPUTATIONAL METHODS

A. Density-density response function

In static linear response theory [14,28,29], the density-density response function $\chi(\mathbf{r},\mathbf{r}')$ describes the change of the charge density δn at position $\mathbf{r}$ if the external potential δv_{ext} undergoes a small change at $\mathbf{r}'$ so that $\chi(\mathbf{r},\mathbf{r}') = \delta n(\mathbf{r})/\delta v_{\text{ext}}(\mathbf{r}')$. For our study, we start by calculating the independent-particle density-density response function $\chi^0(\mathbf{r},\mathbf{r}')$. To illustrate this quantity, we use a 7-aGNR, which is the smallest ribbon fabricated up to date [30,31], as an example. We choose a supercell size of 1.72 nm × 0.85 nm and calculate the band structure of the ribbon using empirical pseudopotentials [32]. We use an energy cutoff of 10 Ry, resulting in 2237 plane waves in the basis set. Applying first-order perturbation theory [14,33,34], the static independent-particle polarizability matrix is calculated as

$$\chi^0_{\mathbf{G}\mathbf{G}'}(\mathbf{q}) = \frac{4}{\Omega}\sum_{c,v,\mathbf{k}} \frac{\langle v,\mathbf{k}|e^{-i(\mathbf{q}+\mathbf{G})\cdot\mathbf{r}}|c,\mathbf{k}+\mathbf{q}\rangle\langle c,\mathbf{k}+\mathbf{q}|e^{i(\mathbf{q}+\mathbf{G}')\cdot\mathbf{r}'}|v,\mathbf{k}\rangle}{E^v_{\mathbf{k}} - E^c_{\mathbf{k}+\mathbf{q}}} \tag{1}$$

using the eigenvalues $E^n_{\mathbf{k}}$ $(n = c,v)$ and eigenfunctions $|n,\mathbf{k}\rangle$ obtained from the calculation of the band structure. In Eq. (1), $\mathbf{G}$ and $\mathbf{G}'$ are reciprocal lattice vectors, $\mathbf{q}$ and $\mathbf{k}$ are the vectors within the first Brillouin zone, and Ω denotes the crystal volume. Since vacuum separates the aGNRs along the width direction x and the direction perpendicular to the surface y, $\chi^0_{\mathbf{G}\mathbf{G}'}(\mathbf{q})$ does not depend on q_x or q_y. Along the periodic direction of the ribbon z we choose to deal only with long-wavelength perturbing electric fields (i.e., $q_z \to 0$). The "head," "wing," and "body" elements of the polarizability matrix when $q_z \to 0$ are calculated following Ref. [14]. We sum over all of the 30 valence bands and over 800 conduction bands [35]. The first Brillouin zone is discretized with 20 k_z points along z.

We obtain $\chi^0(\mathbf{r},\mathbf{r}')$ by transforming $\chi^0_{\mathbf{G}\mathbf{G}'}(q_z \to 0)$ to real space as

$$\chi^0(\mathbf{r},\mathbf{r}') = \frac{1}{\Omega_{\text{cell}}}\sum_{\mathbf{G}\mathbf{G}'} e^{i\mathbf{G}\mathbf{r}}\chi^0_{\mathbf{G}\mathbf{G}'}(q_z \to 0)e^{-i\mathbf{G}'\mathbf{r}'}, \tag{2}$$

where Ω_{cell} is the supercell volume. Within the random-phase approximation (RPA), $\chi^0(\mathbf{r},\mathbf{r}')$ equals the screened response function $P(\mathbf{r},\mathbf{r}')$, which relates the induced charge $\rho_{\text{ind}}(\mathbf{r})$ to the total potential $\varphi_{\text{tot}}(\mathbf{r})$ through

$$\rho_{\text{ind}}(\mathbf{r}) = e^2\int P(\mathbf{r},\mathbf{r}')\varphi_{\text{tot}}(\mathbf{r}')d\mathbf{r}', \tag{3}$$

where e is the elemental electron charge. The function $\chi^0(\mathbf{r},\mathbf{r}')$, averaged along z, is shown in Fig. 1 for a perturbation at $\mathbf{r}'$, for $\mathbf{r}'$ is at the ribbon center (a) and at the bottom-left vacuum region (b), respectively. Two important features of the density-density response function are its exponential spatial decay, like the electron density, and its scalar nature. The first feature enables us to employ a small supercell—as long as it is sufficiently large to guarantee the independence of the

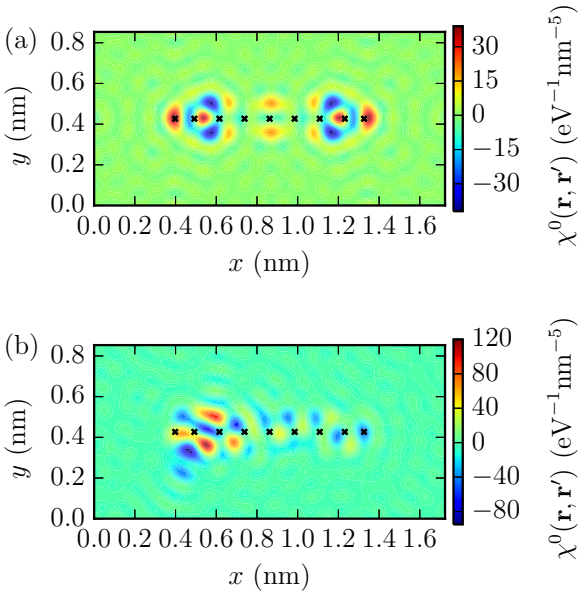

FIG. 1. The independent-particle density-density response function $\chi^0(\mathbf{r},\mathbf{r}')$ of a 7-aGNR in response to a long-wavelength perturbing electric field $q_z \to 0$, (a) when the perturbation $\mathbf{r}'$ is at the ribbon center [i.e., $\mathbf{r}' = (0.86\text{ nm}, 0.43\text{ nm})$], and (b) when the perturbation $\mathbf{r}'$ is at the bottom-left vacuum [i.e., $\mathbf{r}' = (0.43\text{ nm}, 0.21\text{ nm})$]. The microscopic distribution of polarization charge can be observed. The seven carbon atoms in the center of the ribbon and the two terminating hydrogen atoms on the edges are indicated with the black cross symbols.

calculated band structure on its size—to study the dielectric response.

B. Microscopic Poisson equation

A microscopic Poisson equation follows from the relationship between the induced charge and the total potential:

$$\epsilon_0 \nabla^2 \varphi_{\rm tot}(\mathbf{r}) + e^2 \int P(\mathbf{r},\mathbf{r}')\varphi_{\rm tot}(\mathbf{r}')d\mathbf{r}' = -\rho_{\rm ext}(\mathbf{r}), \quad (4)$$

where ϵ_0 is the vacuum permittivity and $\rho_{\rm ext}(\mathbf{r})$ is the external charge. Equation (4) is obtained by combining Gauss's law $\nabla \cdot \mathcal{E}_{\rm tot}(\mathbf{r}) = \rho_{\rm tot}(\mathbf{r})/\epsilon_0 = [\rho_{\rm ext}(\mathbf{r}) + \rho_{\rm ind}(\mathbf{r})]/\epsilon_0$, with the relation between the electric field $\boldsymbol{E}_{\rm tot}(\mathbf{r}) = -\nabla\varphi_{\rm tot}$, in the Coulomb gauge and using Eq. (3) to express the induced charge as a function of the total potential. Equation (4) effectively presents us a microscopic Poisson equation which can be straightforwardly discretized and solved when Dirichlet/Neumann/periodic boundary conditions are applied. Under the assumption of linear response and the RPA, solving the microscopic Poisson equation with $\chi^0(\mathbf{r},\mathbf{r}')$ yields the exact microscopic total potential.

Whereas the total potential is obtained by solving the microscopic Poisson equation, the contributions of the external potential and the induced potential are not immediately evident. Since the aGNR is surrounded by vacuum, the induced charge density is contained in the aGNR and can be calculated using Eq. (3). From the knowledge of the induced charge density, we can calculate the induced potential as

$$\varphi_{\rm ind}(\mathbf{r}) = \int \frac{\rho_{\rm ind}(\mathbf{r}')}{4\pi\epsilon_0|\mathbf{r}-\mathbf{r}'|}d\mathbf{r}'. \quad (5)$$

Once the induced potential is determined, the external perturbing potential can be obtained by subtracting the induced potential from the total potential. The electric fields (external, induced, and total) are then calculated as the negative gradients of the respective potential. For a 2D charge distribution after averaging along z, the 2D Coulomb kernel rather than the 3D Coulomb kernel should be used and the induced potential is determined as

$$\varphi_{\rm ind}(\mathbf{r}) = \int \frac{\rho_{\rm ind}(\mathbf{r}')\ln(|\mathbf{r}-\mathbf{r}'|/L)}{2\pi\epsilon_0}d\mathbf{r}', \quad (6)$$

where L is an arbitrary scaling length. In practice, to avoid integrating over the singularity of $\ln(|\mathbf{r}-\mathbf{r}'|/L)$, we can calculate the induced potential by placing the induced charge in a much larger simulation region. We transform the induced charge to reciprocal space using the Fourier transform $\rho_{\rm ind}(\mathbf{r}) \rightarrow \rho_{\rm ind}(\mathbf{q})$, and obtain the potential as $\varphi_{\rm ind}(\mathbf{q}) = \rho_{\rm ind}(\mathbf{q})/(4\pi\epsilon_0|\mathbf{q}|^2) \rightarrow \varphi_{\rm ind}(\mathbf{r})$.

C. Microscopic dielectric tensor

To compute a microscopic dielectric tensor, we apply Eq. (4) to two nanocapacitors, a "horizontal" one with the plates parallel to the aGNR surface and a "vertical" one with the plates perpendicular to the aGNR surface. For the horizontal nanocapacitor we apply the potential perturbation by imposing 1 V on the top plate and −1 V on the bottom plate. Periodic boundary conditions are applied on the left and right boundaries. There is no free charge inside the capacitor. By solving Eq. (4) in the two-dimensional case, we obtain the total potential and the induced charge density whose distributions are shown in Fig. 2. We can observe the curved potential distribution around the nanoribbon region from Fig. 2(a). The microscopic induced-charge distribution forming a dipole can be seen in Fig. 2(b). Similarly, we determine the potential and induced charge for the vertical nanocapacitor (not shown).

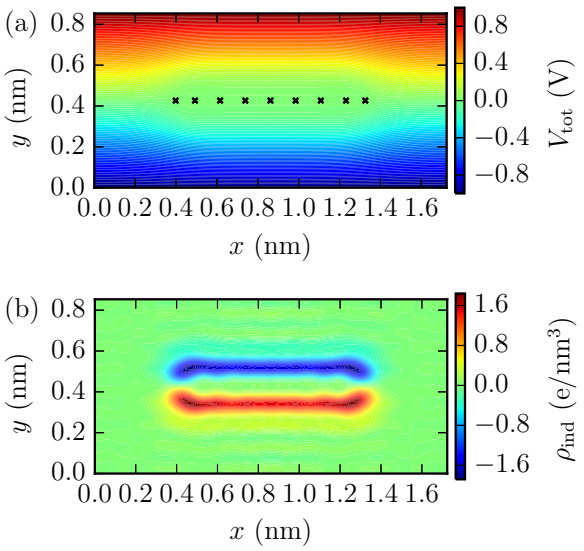

FIG. 2. The total potential (a) and the induced charge density (b) for a "horizontal" parallel-plate capacitor when 1 V is applied to the top plate and −1 V to the bottom plate. In response to the external field, a dipole is formed which counteracts the external electric field with a polarization field.

Having obtained $\varphi_{\rm tot}(\mathbf{r})$ and $\rho_{\rm ind}(\mathbf{r})$, we calculate the respective microscopic external electric field and total electric field for the horizontal ($\mathcal{E}^{\rm hor}_{\rm ext/tot}$) and the vertical ($\mathcal{E}^{\rm ver}_{\rm ext/tot}$) capacitor. The microscopic dielectric tensor of a 1D nanostructure in the confined (x,y) plane (i.e., the transverse dielectric tensor) is then evaluated as

$$\begin{bmatrix} \epsilon_r^{xx}(\mathbf{r}) & \epsilon_r^{xy}(\mathbf{r}) \\ \epsilon_r^{yx}(\mathbf{r}) & \epsilon_r^{yy}(\mathbf{r}) \end{bmatrix} = \begin{bmatrix} \mathcal{E}^{\rm hor}_{{\rm ext},x}(\mathbf{r}) & \mathcal{E}^{\rm ver}_{{\rm ext},x}(\mathbf{r}) \\ \mathcal{E}^{\rm hor}_{{\rm ext},y}(\mathbf{r}) & \mathcal{E}^{\rm ver}_{{\rm ext},y}(\mathbf{r}) \end{bmatrix} \begin{bmatrix} \mathcal{E}^{\rm hor}_{{\rm tot},x}(\mathbf{r}) & \mathcal{E}^{\rm ver}_{{\rm tot},x}(\mathbf{r}) \\ \mathcal{E}^{\rm hor}_{{\rm tot},y}(\mathbf{r}) & \mathcal{E}^{\rm ver}_{{\rm tot},y}(\mathbf{r}) \end{bmatrix}^{-1}, \quad (7)$$

where $\mathcal{E}^{\rm hor/ver}_{\rm ext/tot,x/y}(\mathbf{r})$ is the x or y component of the external/total electric field for the horizontal/vertical nanocapacitor and $\epsilon_r^{ij}(\mathbf{r})$ $(i,j = x,y)$ is a component of the dielectric tensor which indicates the dielectric response along the direction i when the perturbing electric field is applied along the direction j.

III. RESULTS AND DISCUSSION

A. Microscopic dielectric tensor of a 7-aGNR

From the total potential and the induced-charge density of a 7-aGNR, shown in Fig. 2, we calculate the microscopic dielectric tensor using Eq. (7) and each component of the tensor is shown in Fig. 3. The anisotropy of the microscopic dielectric properties can be observed. Observing the distribution of both $\epsilon_r^{xx}(\mathbf{r})$ and $\epsilon_r^{yy}(\mathbf{r})$, the ribbon region exhibits a large

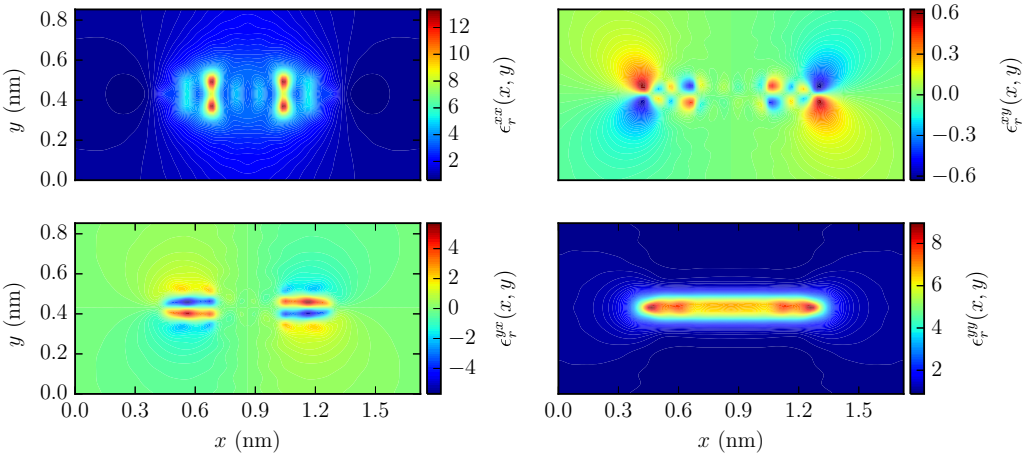

FIG. 3. The microscopic dielectric tensor of a 7-aGNR in vacuum. The top-left figure and bottom-right figure show the diagonal components and the top-right figure and bottom-left figure show the off-diagonal components.

microscopic dielectric constant, whereas it approaches ϵ_0 in the vacuum region. Nevertheless, inside the ribbon, $\epsilon_r^{xx}(\mathbf{r})$ exhibits more pronounced microscopic oscillations compared to $\epsilon_r^{yy}(\mathbf{r})$. The off-diagonal elements of the microscopic dielectric tensor $\epsilon_r^{xy}(\mathbf{r})$ and $\epsilon_r^{yx}(\mathbf{r})$ obviously exhibit the inversion symmetry of the aGNR. Macroscopically, the off-diagonal elements of the macroscopic dielectric tensor vanish. This is the consequence of the fact that x and y are two of the three principal axes of the nanosystem. Our results for the microscopic dielectric tensor show that no long-range Coulomb kernel or mirror-image effects are present when using the density-density response function and the vacuum permittivity is recovered even using a relatively small supercell. Unfortunately, this is not the case when we wish to calculate the dielectric matrix $\epsilon^{-1}_{\mathbf{GG}'}(\mathbf{q})$. A direct calculation of the permittivity from $\epsilon^{-1}_{\mathbf{GG}'}(\mathbf{q})$ requires the use of a large supercell [9,26] and/or a truncated Coulomb kernel [27] to minimize the long-range Coulomb interaction between the real dipole and the image dipoles.

B. Ribbon-width dependence of dielectric permittivity

To investigate the size dependence of the out-of-plane microscopic dielectric constant $\epsilon_r^{yy}(\mathbf{r})$, we also simulate a 3-aGNR, a 5-aGNR, and a 6-aGNR. Using empirical pseudopotentials, we find for each of these ribbons a band gap of 1.19, 0.43, and 1.03 eV, respectively, in contrast to the band gap of 1.70 eV for the 7-aGNR. The distribution of $\epsilon_r^{yy}(\mathbf{r})$ along the horizontal plane of these ribbons is plotted in Fig. 4 [36]. The permittivities in the center of all ribbons, except the 3-aGNR, are approximately $6\epsilon_0$ and the permittivities on the ribbon edges show similar peaks and valleys oscillating around $7\,\epsilon_0$. These features show that band gap barely affects the out-of-plane microscopic dielectric constant. This suggests that the matrix elements in Eq. (1) corresponding to dipole transitions from the valence band maximum to the conduction band minimum do not dominate the polarizability. Rather, it indicates that the dipole transitions from valence bands to high-energy conduction bands are equally important [10].

Previous studies have showed that the macroscopic transverse susceptibility tensor of carbon nanotubes depends on their diameter but not on the band gap [8,9,37,38]. This independence on the chirality and energy band gap was attributed to selection rules forcing the matrix element of Eq. (1) to be zero for the valence bands and conduction bands near the band gap. It was also shown that the macroscopic (i.e., averaged) dielectric constant of nanostructures was reduced as their size (e.g., the radius of quantum dots or the thickness of silicon thin films) decreased [1–5,11,39]. However, this was attributed to a surface effect [1,5,40], rather than to the commonly assumed quantum-confinement and band-gap effect [11,41,42].

C. Microscopic dielectric permittivity of graphene

To enable a direct comparison of the microscopic dielectric constant $\epsilon_r^{yy}(\mathbf{r})$ of the GNRs with that of graphene, as for aGNRs, we build a nanocapacitor with graphene as dielectric and the capacitor plates are parallel to the graphene surface. We apply the potential perturbation by imposing a voltage on the plates. By solving the microscopic Poisson equation, we obtain the induced charge density.

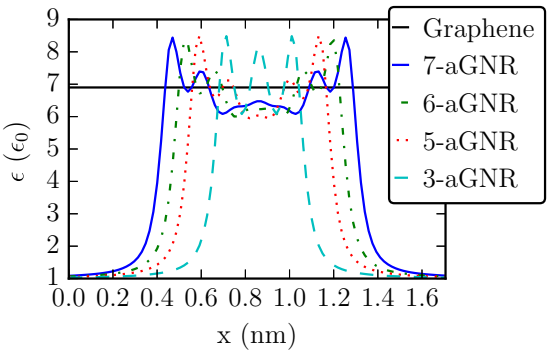

FIG. 4. Out-of-plane microscopic dielectric constant $\epsilon_r^{yy}(\mathbf{r})$ in the horizontal plane for different ribbon widths. The local permittivity in the interior of all ribbons except for the 3-aGNR shows values close to $6\epsilon_0$. The local permittivities on the ribbon edges show similar oscillating peaks. The black horizontal straight line $\epsilon = 6.9\epsilon_0$ is the macroscopic dielectric constant of graphene at the carbon-atom plane, as shown in Fig. 5.

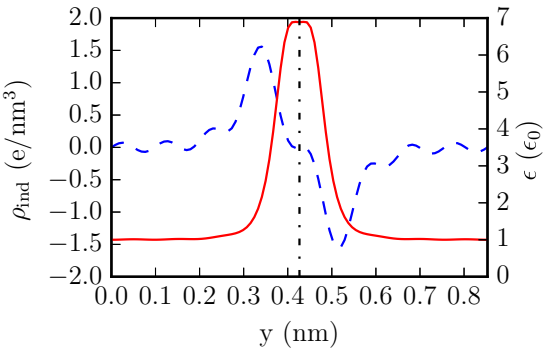

FIG. 5. Induced charge density (left y axis, dashed blue line) when a voltage $U = 2$ V is applied to the graphene nanocapacitor and the microscopic dielectric constant of graphene along the direction perpendicular to the graphene plane (right y axis, solid red line). In response to the potential perturbation, a dipole is formed across the graphene plane, as shown by the induced charge density. The microscopic dielectric permittivity exhibits a peak value of $6.9\,\epsilon_0$ on the carbon-atom plane and decays to the vacuum permittivity about 0.1 nm away from the carbon-atom plane, indicated by the dashed vertical line.

The induced charge density averaged on the (x,z) plane is shown in Fig. 5. The long-range oscillations of the induced charge are caused by local-field effects [7]. The polarization profile along y can be calculated by applying Gauss's law in 1D [43]. Thus, the microscopic dielectric constant of graphene along y can be determined straightforwardly and it is also shown in Fig. 5. The microscopic dielectric permittivity decays from $6.9\,\epsilon_0$ in the carbon-atom plane to the vacuum permittivity within approximately 0.1 nm. This shows that the out-of-plane dielectric permittivity of the aGNRs resembles that of graphene.

We also evaluate the capacitance per unit area of the graphene nanocapacitor as D/U, where D is the displacement field and U is the applied voltage. We find a capacitance of 13.28 F/m^2. Equivalently, attributing an effective dielectric thickness d and a macroscopic dielectric constant $\epsilon_{\rm mac}$ to graphene, the capacitance can also be calculated as $U/D = d/\epsilon_{\rm mac} + (d_0 - d)/\epsilon_0$ (d_0 is the distance between the capacitor plates) since graphene and vacuum are connected in series. Assuming $\epsilon_{\rm mac} = 6.9\epsilon_0$, the effective dielectric thickness of graphene is about 0.22 nm. This corresponds roughly to the

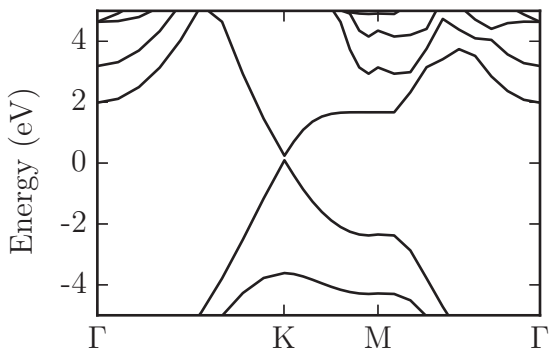

FIG. 6. Band structure of a monolayer hBN-graphene heterostructure using empirical pseudopotentials.

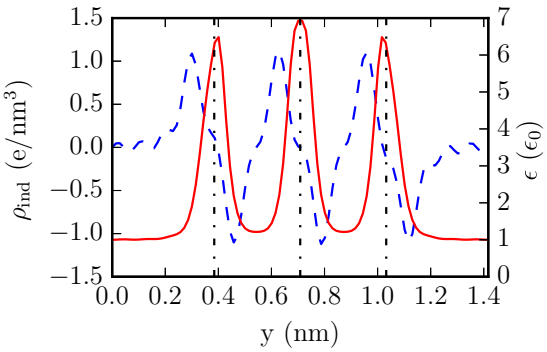

FIG. 7. The induced charge density (left y axis, dashed blue line) when a voltage $U = 2$ V is applied on the hBN-graphene-hBN heterostructure and the microscopic dielectric constant of the heterostructure along the direction perpendicular to the graphene plane (right y axis, solid red line). The dashed vertical line in the middle represents the carbon-atom plane of graphene and the dashed vertical lines on the sides represent the atomic plane of the monolayer hBN.

distance of the center of the respective induced-charge layer comprising the dipole shown in Fig. 5.

D. Surrounding dielectric effect on graphene

To elucidate the impact of surrounding dielectrics on the dielectric constant of graphene, we study the case of a hBN-graphene-hBN heterostructure. Such a heterostructure is considered for applications in future nanoelectronics [44–47]. Referring to the literature [48], the stacking sequence is AaA and the equilibrium distance between the monolayer hBN and graphene is set to 0.324 nm. The in-plane lattice constant is assumed to be 0.246 nm for both graphene and hBN. We determine the empirical pseudopotentials of boron and nitrogen assuming that they have the same form as the pseudopotential of the carbon atom [32]. Fitting the parameters so that the calculated band structure of the monolayer hBN-graphene heterostructure (shown in Fig. 6) resembles the one calculated with the plane-wave density-functional theory package, Vienna *ab initio* simulation package (VASP) [49–52], we obtain $v_{\rm B}(q) = 1.01(0.3q^2 - 1.424)/(e^{0.3q^2-0.938} + 1)$ and $v_{\rm N}(q) = 1.95(0.354q^2 - 1.65)/(e^{0.354q^2-0.938} + 1)$ (in atomic units), for B and N, respectively.

The atomic-scale dielectric permittivity of the hBN-graphene-hBN heterostructure is calculated and shown in Fig. 7. Comparing it to Fig. 5, we see that the dielectric constant of graphene is barely affected by the hBN layers and the macroscopic dielectric constant of the monolayer hBN is around $6.4\,\epsilon_0$. In the interlayer region between graphene and the hBN layers, the dielectric constant decays quickly to the vacuum permittivity due to the screening effect of the polarization charge induced in each layer.

IV. CONCLUSION

We have presented a microscopic Poisson equation which provides a way to calculate the microscopic dielectric tensor of 1D nanostructures and the out-of-plane microscopic dielectric constant of 2D nanostructures. We have studied the

ribbon-width dependence of the dielectric constant of aGNRs and found that the width and the related band gap barely affect the out-of-plane microscopic dielectric constant. We have also shown the atomic-scale dielectric permittivity of graphene and calculated the effective dielectric thickness of graphene to be 0.22 nm for a dielectric constant of $6.9\,\epsilon_0$. We investigated the effect of a surrounding monolayer hBN dielectric on the dielectric constant of graphene and concluded that the effect was minor because of the screening by the induced charge.

As demonstrated, a direct solution of the microscopic Poisson equation incorporates all quantum effects on the electrostatics. This provides a physically sound avenue for atomistic quantum transport simulation in nanotransistors by solving the Schrödinger equation and the microscopic Poisson equation self-consistently without the necessity of knowing the dielectric tensor of the nanosystems. When simulating aGNR field-effect transistors which may have electrostatic configurations other than the two capacitors considered here, the microscopic Poisson equation [Eq. (4)] can be solved again. Alternatively, the microscopic dielectric tensor shown in Fig. 3 provides a rigorous replacement for the previously used uniform dielectric constant assumption in Refs. [18,20] or the box assumption in Refs. [21–23] when solving the "ordinary" Poisson equation $\nabla \cdot [\epsilon(\mathbf{r})\nabla\varphi_{\text{tot}}(\mathbf{r})] = -\rho_{\text{ext}}(\mathbf{r})$.

ACKNOWLEDGMENTS

This work has been supported by a Nanoelectronics Research Initiative/South West Academy of Nanoelectronics (SRC/NRI Theme 2400.011) grant.

[1] C. Delerue, M. Lannoo, and G. Allan, Phys. Rev. B **68**, 115411 (2003).
[2] F. Giustino and A. Pasquarello, Phys. Rev. B **71**, 144104 (2005).
[3] J. Nakamura, S. Ishihara, A. Natori, T. Shimizu, and K. Natori, J. Appl. Phys. **99**, 054309 (2006).
[4] G. Zhang, M.-B. Yu, C.-H. Tung, and G.-Q. Lo, IEEE Electron Device Lett. **29**, 1302 (2008).
[5] X. Cartoixà and L.-W. Wang, Phys. Rev. Lett. **94**, 236804 (2005).
[6] K. Kunc and R. Resta, Phys. Rev. Lett. **51**, 686 (1983).
[7] R. Resta and K. Kunc, Phys. Rev. B **34**, 7146 (1986).
[8] L. X. Benedict, S. G. Louie, and M. L. Cohen, Phys. Rev. B **52**, 8541 (1995).
[9] B. Kozinsky and N. Marzari, Phys. Rev. Lett. **96**, 166801 (2006).
[10] I. Vasiliev, S. Öğüt, and J. R. Chelikowsky, Phys. Rev. Lett. **78**, 4805 (1997).
[11] L.-W. Wang and A. Zunger, Phys. Rev. Lett. **73**, 1039 (1994).
[12] B. Meyer and D. Vanderbilt, Phys. Rev. B **63**, 205426 (2001).
[13] S. Baroni and R. Resta, Phys. Rev. B **33**, 7017 (1986).
[14] M. S. Hybertsen and S. G. Louie, Phys. Rev. B **35**, 5585 (1987).
[15] In literature, the terms "susceptbility" and "polarizabiity" are not consistently employed. In Refs. [16,17] the authors use polarizability to relate the induced dipole moment to the electric field, which are normally used for molecules or semiconductor clusters. Here we use polarizability to relate the charge response to a change of the potential. Thus, the term polarizability used in Refs. [16,17] is referred to as susceptibility, although, strictly speaking, electrical susceptibility relates the polarization to the electric field.
[16] Y. P. Tan, M. Povolotskyi, T. Kubis, T. B. Boykin, and G. Klimeck, Phys. Rev. B **92**, 085301 (2015).
[17] N. A. Bruque, R. R. Pandey, and R. K. Lake, Phys. Rev. B **76**, 205322 (2007).
[18] J. Fang, W. G. Vandenberghe, B. Fu, and M. V. Fischetti, J. Appl. Phys. **119**, 035701 (2016).
[19] J. Fang, W. Vandenberghe, and M. Fischetti, in *Proceedings of the 2015 International Workshop on Computational Electronics, West Lafayette, IN*, edited by G. Klimeck (IEEE, New York, 2015), pp. 1–3.
[20] J. Fang, W. G. Vandenberghe, and M. V. Fischetti, in *Proceedings of the 2015 International Conference on Simulation of Semiconductor Processes and Devices, Washington DC*, edited by N. Goldsman (IEEE, New York, 2015), pp. 84–87.
[21] J. Guo, Nanoscale **4**, 5538 (2012).
[22] Y. Ouyang, Y. Yoon, and J. Guo, IEEE Trans. Electron Device **54**, 2223 (2007).
[23] G. Fiori and G. Iannaccone, IEEE Electron Device Lett. **28**, 760 (2007).
[24] L. Fu, E. Yaschenko, L. Resca, and R. Resta, Phys. Rev. B **60**, 2697 (1999).
[25] L. Bengtsson, Phys. Rev. B **59**, 12301 (1999).
[26] R. Ramprasad and N. Shi, Phys. Rev. B **72**, 052107 (2005).
[27] S. Ismail-Beigi, Phys. Rev. B **73**, 233103 (2006).
[28] R. Del Sole and E. Fiorino, Phys. Rev. B **29**, 4631 (1984).
[29] J. Harl, Ph.D. dissertation, University of Vienna, Vienna, Austria, 2008.
[30] J. Cai *et al.*, Nature (London) **466**, 470 (2010).
[31] H. Huang, D. Wei, J. Sun, S. L. Wong, Y. P. Feng, A. H. C. Neto, and A. T. S. Wee, Sci. Rep. **2**, 983 (2012).
[32] Y. Kurokawa, S. Nomura, T. Takemori, and Y. Aoyagi, Phys. Rev. B **61**, 12616 (2000).
[33] S. L. Adler, Phys. Rev. **126**, 413 (1962).
[34] N. Wiser, Phys. Rev. **129**, 62 (1963).
[35] Convergence tests show that for $\mathbf{G}$ and $\mathbf{G}'$ vectors of small magnitude, the element $\chi^0_{\mathbf{GG}'}$ converges rapidly with respect to the number of conduction bands summed in Eq. (4). For $\mathbf{G}$ or $\mathbf{G}'$ vectors with the largest magnitude, $\chi^0_{\mathbf{GG}'}$ converges slowly. Nevertheless, the microscopic dielectric constant, which will be discussed later, reaches a satisfactory convergence when 800 conduction bands are used to calculate the polarizability, if one sets the microscopic dielectric constant calculated using 2207 conduction bands as the reference.
[36] The supercell size is assumed to be the same. The polarizabilities of these ribbons are calculated with summing over all the valence bands of each ribbon, the same number of 800 conduction bands, and the same number of 20 k_z points.
[37] G. Y. Guo, K. C. Chu, D.-s. Wang, and C.-g. Duan, Phys. Rev. B **69**, 205416 (2004).
[38] E. N. Brothers, K. N. Kudin, G. E. Scuseria, and C. W. Bauschlicher, Phys. Rev. B **72**, 033402 (2005).
[39] H. G. Yoo and P. M. Fauchet, Phys. Rev. B **77**, 115355 (2008).
[40] M. v. Lauve, Ann. Phys. (Berlin) **349**, 1197 (1914).
[41] D. R. Penn, Phys. Rev. **128**, 2093 (1962).
[42] T. Moss, Phys. Status Solidi (b) **131**, 415 (1985).
[43] N. Shi and R. Ramprasad, Phys. Rev. B **74**, 045318 (2006).

[44] G. Giovannetti, P. A. Khomyakov, G. Brocks, P. J. Kelly, and J. van den Brink, Phys. Rev. B **76**, 073103 (2007).
[45] J. Sławińska, I. Zasada, and Z. Klusek, Phys. Rev. B **81**, 155433 (2010).
[46] S. Bruzzone, D. Logoteta, G. Fiori, and G. Iannaccone, Sci. Rep. **5**, 14519 (2015).
[47] G. Shi, Y. Hanlumyuang, Z. Liu, Y. Gong, W. Gao, B. Li, J. Kono, J. Lou, R. Vajtai, P. Sharma *et al.*, Nano Lett. **14**, 1739 (2014).
[48] Y. Sakai, T. Koretsune, and S. Saito, Phys. Rev. B **83**, 205434 (2011).
[49] G. Kresse and J. Furthmüller, Phys. Rev. B **54**, 11169 (1996).
[50] P. E. Blöchl, Phys. Rev. B **50**, 17953 (1994).
[51] H. J. Monkhorst and J. D. Pack, Phys. Rev. B **13**, 5188 (1976).
[52] J. P. Perdew, K. Burke, and M. Ernzerhof, Phys. Rev. Lett. **77**, 3865 (1996).